ELASTIC STIFFNESS OF FRACTURED ROCK WITH MULTIPLE FRACTURE-FILLING MATERIALS

Kyle T. Spikes

Department of Geological Sciences
The University of Texas at Austin

ABSTRACT

This work is presentation of three statistical rock-physic techniques based on well data observations that explains the minimal or lack of azimuthally varying velocities in known horizontal transverse isotropic gas shales. These modeling approaches include a factor of cement either in the fracture pore space or in the background material. The Hudson fracture model is extended in each modeling technique to relate the elastic moduli to the cement content, as a function of fracture aspect ratio and fracture density. The stochastic nature of the first two techniques arises from simulations of distributions of cement volume, fracture shape, and fracture density. For the third method, the statistical scheme comes from simulating distributions of background matrix moduli as a function of cement volume. Uncertainty accompanies these moduli, and this uncertainty decreases as cement quantity increases. Accordingly, these inputs enable the rock-physics model to be treated statistically through multiple realizations. Modeling results illustrate that P- and S-waves parallel and perpendicular to fractures overlap noticeably. This overlap becomes more significant as the cement volume increases. The techniques and accompanying results demonstrated that some fractures could be cemented. Just a few cemented fractures increase the velocity perpendicular to the fractures, which reduces or eliminates the azimuthal dependence. This modeling may help reconcile the issue that azimuthal velocity variations are measurable in surface seismic data, but in well-log data, the cement content masks or even eliminates directionally dependent velocity.

INTRODUCTION

This work addresses a relatively common observation from dipole sonic log data recorded in gas formations. Specifically, in gas shales known to be fractured including the Marcellus Shale (Engelder et al., 2009) and the Woodford Shale, (Portas, 2010; Andrews, 2009), the fast and slow S-waves show little to no difference as a function of azimuth (Figure 1). However, surface seismic observations indicate azimuthal velocity variations (Engelder et al., 2009), with the expectation that vertical fractures induce the HTI behavior. These scale-dependent observations must be reconciled if both data types are to be used properly in quantitative seismic interpretation. Several plausible reasons for this exist. The simplest is that the rock around the wellbore (within several wavelengths) contains no fractures. In this situation, an isotropic or a VTI medium could be in place (VTI due to layering), so the observed shear-wave data senses no

azimuthal anisotropy. More complex, an orthorhombic medium may be present with horizontal layering and vertical fractures. In this case, velocity measurements may show isotropic or nearly isotropic behavior because the effects of the high-order symmetry are quite small. Each scenario very well may exist with equal probability.
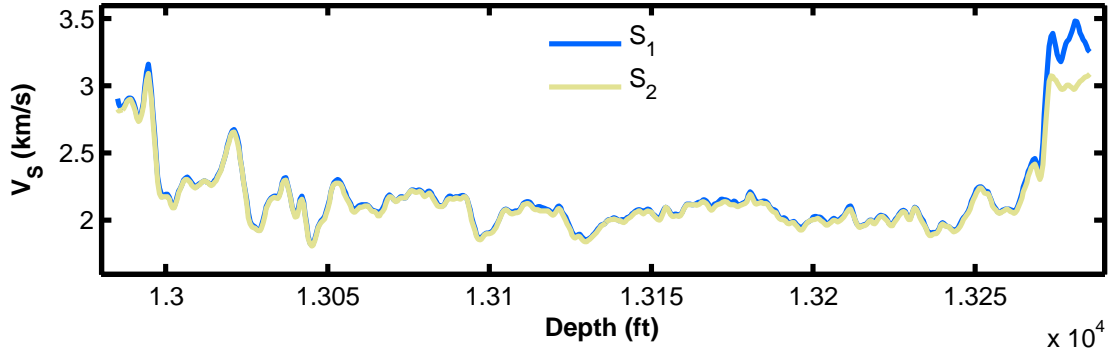

Figure 1. S-wave velocity measurements fast (S1) and slow (S2) from the Woodford shale. This clearly demonstrates the problem addressed in this work where minimal difference exists in the two S-wave velocities from a shale known to contain fractures.

One more possibility exists, which is the topic of this work. That situation includes vertical fractures where some are open and fluid filled and some are cemented. The hypothesis for this work is that the propagating waves sense a series of open and cemented fractures. A common approach to assess the how fractures influence the effective stiffness is to assume that these fractures or cavities are embedded in an isotropic background material. These models all follow the solving of an effective stress tensor based on Eshelby (1957). Other techniques include Kuster and Toksöz (1974), Budianksy and O'Connell (1976), Hudson (1980), Norris (1987), and Jakobsen et al. (2003). All these approaches represent this medium as homogeneous and HTI. In the case of multiple fracture-filling materials, the HTI medium becomes heterogeneous.

Considering the Marcellus and Woodford Shales, the true nature of the rock may be orthorhombic and heterogeneous. The stiffness tensor for an orthorhombic medium requires nine independent elastic constants. When heterogeneity is included, those nine constants vary in space. The corresponding forward problem is difficult, and the inverse problem is intractable because of the lack of requisite measurements. The Hudson (1980) model, differential effective media (DEM), and the T-matrix approaches simplify this orthorhombic system typically to a lower-order symmetry, most often to transverse isotropy. In doing so, the forward problems can be solved if the elastic moduli are provided for the background material, the fracture-filling material and their proportions as well as fracture shape and fracture density.

Identifying fracture shapes, density, and orientation from seismic data is important because they potentially indicate locations of enhanced productivity and preferential directional permeability. The presence of cemented fractures may limit this productivity or alter the permeability tensor. The Marcellus and Woodford Shales have been analyzed in terms of azimuthal anisotropy (Engelder et al., 2009) and log data for brittleness (e.g., Kahraman, 2002). The methodology presented here, based on well-log data, is a statistical rock-physics technique to model a rock with HTI symmetry. It complements the work on the Woodford and Marcellus

Shales. Furthermore, it explains shear-wave velocity measurements that are quite similar although evidence suggests that the fast and slow S-waves should be notably different.

This work employs a numerical rock-physics model, the Hudson (1980) model. This model adds anisotropic corrections to isotropic stress tensor elements. Inputs into the model include moduli for the background material, fracture aspect ratio, fracture density, and moduli for the fracture filling material. The model is used in three different ways, each having its own statistical nature, and in each case, cement is introduced. First, a portion of the fractures is assigned to contain cement and the remainder to contain a fluid. This is the same as using an effective material is treated as a mixture of cement and fluid, along with input distributions of fracture aspect ratio and fracture density. Second, two sets of anisotropic corrections are superimposed. One set corresponds to fluid-filled fractures and the other to cement-filled. The summation provides an effective anisotropic stress tensor. The fracture porosity contains both fluid and cement. Third, the cement is treated as part of the background material. Cement is correlated with the background stiffness, fracture aspect ratio, and fracture density.

Deterministic rock-physics models can be used in a probabilistic or stochastic sense by treating one or more inputs into those models as distributions (Avseth et al., 2005; Doyen, 2007). The purpose of implementing a statistical formulation is to obtain estimates of uncertainty of real data associated with measurement errors and natural variability in the rock. It also provides an estimate of the accuracy of the deterministic model. For the three approaches, inputs into the Hudson model are distributions. Results from each procedure indicate that small fractions of cement reduce the expected HTI behavior within the range of modeled uncertainty. Application of this work to field seismic data could play a role in explaining azimuthal anisotropy observations, or lack of them. It could also provide constraints on directional permeability calculations. Importantly, the modeling techniques presented here could help reconcile differences in seismic and well-bore measurements in some gas shale formations.

THEORY

The basis for many effective medium theories comes from the solution of Eshelby (1957). This particular formulation and solution comes from embedding a single ellipsoidal inclusion into an isotropic, homogeneous medium. The solution is exact for the static strain inside the inclusion, and it is dependent on either constant applied stress or strain. Computation of the effective elastic moduli (Equation 1) requires the potential energy of the total system of volume V, with a constant applied strain e^A.

$$\frac{1}{2}c_{ij}^* e_i^A e_j^A V = \frac{1}{2}c_{ij}^0 e_i^A e_j^A V + E_{incl} \tag{1}$$

The presence of the crack causes a change in the energy: E_{incl}. This can be rewritten in terms of the inclusion volume (V_{incl}) and the stress-free strain of the inclusion (e_j^T). To restore the inclusion to its original shape after applying e^A, this stress-free strain is needed. The end result is the corrections of the isotropic c_{ij}^0 to an effective anisotropic tensor through anisotropic

corrections (Equation 2). These solutions are the bases for Hudson's (1980, 1981, 1994), and Cheng's (1993), and Nishizawa (1982) models.

$$c_{ij}^{eff} = c_{ij}^0 - \phi c_{ij}^1 \tag{2}$$

where ϕ is the porosity.

The Hudson model

Hudson's (1980, 1981) model is presented here to illustrate its limitations and to demonstrate how it is extended to include cement for the work in this paper. It is based analysis of wave scattering theory through an elastic solid. It begins with a solid that contains thin, ellipsoidal cracks or inclusions that are relatively sparse. The effective moduli c_{ij}^{eff} is given by

$$c_{ij}^{eff} = c_{ij}^0 + c_{ij}^1 + c_{ij}^2. \tag{3}$$

In Equation 3, c_{ij}^0 is the background isotropic moduli, c_{ij}^1 are the first-order corrections, and c_{ij}^2 are the second-order corrections. Two independent elastic moduli, λ and μ, describe the background zero-th order correction (Equation 4).

$$c_{ij}^0 = \begin{bmatrix} \lambda + 2\mu & \lambda & \lambda & 0 & 0 & 0 \\ \lambda & \lambda + 2\mu & \lambda & 0 & 0 & 0 \\ \lambda & \lambda & \lambda + 2\mu & 0 & 0 & 0 \\ 0 & 0 & 0 & \mu & 0 & 0 \\ 0 & 0 & 0 & 0 & \mu & 0 \\ 0 & 0 & 0 & 0 & 0 & \mu \end{bmatrix} \tag{4}$$

The corrections made to this, c_{ij}^1 and c_{ij}^2 modify individual components of the effective tensor. A single crack set is considered, with crack normal vectors aligned parallel to the x_3-axis. Only the first-order corrections are needed. The resulting cracked media exhibits horizontal transverse isotropic symmetry. The first-order corrections are

4

$$c_{11}^1 = -\frac{\lambda^2}{\mu}\varepsilon_{cd}U_3$$

$$c_{33}^1 = -\frac{(\lambda + 2\mu)^2}{\mu}\varepsilon_{cd}U_3$$

$$c_{13}^1 = -\frac{\lambda(\lambda + 2\mu)}{\mu}\varepsilon_{cd}U_3 \tag{5}$$

$$c_{44}^1 = -\mu\varepsilon_{cd}U_1$$

$$c_{66}^1 = 0$$

$$\varepsilon_{cd} = \frac{N}{V}a^3 = \frac{3\phi}{4\pi a} = \text{crack density}$$

where a and α are the crack radius and aspect ratio, respectively, and ϕ is the porosity. The terms U_1 and U_3 depend on the crack conditions (Equation 6). Hudson (1994) showed that for dry or fluid-filled cavities (fractures), the formulation is the same as for inclusions (cemented or solid-filled fractures).

$$U_1 = \frac{16}{3}\left(\frac{\lambda + 2\mu}{3\lambda + 4\mu}\right)\left(\frac{1}{1 + M}\right)$$

$$U_3 = \frac{4}{3}\left(\frac{\lambda + 2\mu}{\lambda + \mu}\right)\left(\frac{1}{1 + \kappa}\right) \tag{6}$$

Here, M and κ are

$$M = \frac{4\mu'}{\pi\alpha\mu}\left(\frac{\lambda + 2\mu}{3\lambda + 4\mu}\right)$$

$$\kappa = \left(\frac{K' + \frac{4}{3}\mu'}{\pi\alpha\mu}\right)\left(\frac{\lambda + 2\mu}{\lambda + \mu}\right). \tag{7}$$

K' and μ' are the bulk and shear modulus of the fracture-filling material. Weak inclusions are defined as

$$\frac{\mu\alpha}{K' + \frac{4}{3}\mu'} \approx 1, \tag{8}$$

which is not small enough to be neglected.

For fluid-filled fractures, or fluid-filled cavities, Equations 6 and 7 simplify to

$$M = 0, \quad \kappa = \left(\frac{K'}{\pi \alpha \mu} \right) \left(\frac{\lambda + 2\mu}{\lambda + \mu} \right)$$

$$U_1 = \frac{16}{3} \left(\frac{\lambda + 2\mu}{3\lambda + 4\mu} \right) \tag{8}$$

$$U_3 = \frac{4}{3} \left(\frac{\lambda + 2\mu}{\lambda + \mu} \right) \left(\frac{1}{1 + \kappa} \right).$$

For a case with dry cavities, these reduce further to

$$M = 0, \quad \kappa = 0$$

$$U_1 = \frac{16}{3} \left(\frac{\lambda + 2\mu}{3\lambda + 4\mu} \right) \tag{9}$$

$$U_3 = \frac{4}{3} \left(\frac{\lambda + 2\mu}{\lambda + \mu} \right).$$

Lastly, the density is computed from the porosity as

$$\rho_b = (1 - \phi)\rho_m + \phi \rho_f \tag{10}$$

Three fundamental limitations exist for this model. Hudson (1994) proved that these equations hold for either solid- or fluid-filled inclusions by averaging all shapes and sizes of inclusions. This average mandates that all inclusions contain the same material, and that all inclusions are idealized ellipsoids. Moreover, this system requires an isotropic background (c_{ij}^0), which Nishizawa (1982) pointed out is not always the case. These three assumptions regarding inclusion fill, inclusion shape, and background material are useful but also restrictive. The following extensions presented circumvent the fill and the isotropic background requirements.

Effective fracture-filling material

The approximation presented next is a simple expansion to assign a percentage of the fractures to be cemented, and the remainder of the fractures to be either dry or fluid filled. Importantly, the lack of fractures represents healed or closed fractures. Sayers et al. (2009) dealt with this problem by modifying the normal and tangential compliances of fractures that were bridged locally with cement. Here, the approximation essentially uses an effective fracture-filling material that is a mixture of cement and fluid. The first step divides the fracture density into two parts:

$$\varepsilon_{cd} = \frac{3}{4\pi} \frac{\phi}{\alpha}, \tag{11}$$

where

$$\phi = f_c\phi + (1 - f_c)\phi = \phi_c + \phi_f \tag{12}$$

where f_c is the fraction of cemented fractures, so

$$\varepsilon_{cd} = \frac{3}{4\pi} \frac{(\phi_c + \phi_f)}{\alpha}. \tag{13}$$

The terms with a subscript f refer to the fluid-filled fractures and c to cement-filled fractures. The volume that all the fractures occupy, however, is divided into volumes for fluid-filled and cemented fractures. Aspect ratios are assumed equivalent for both fracture sets of fractures. Then M and κ in Equation 7 become

$$M = \left(\frac{\lambda + 2\mu}{3\lambda + 2\mu}\right)\left(\frac{4}{\pi\mu}\right)\left(\frac{\mu'}{\alpha}\right)$$

$$\kappa = \left(\frac{\lambda + 2\mu}{\lambda + 2}\right)\left(\frac{1}{\pi\mu}\right)\left(\frac{K' + \frac{4}{3}\mu'}{\alpha}\right). \tag{14}$$

Focusing on the far right terms, these are defined as

$$\frac{\mu'}{\alpha} = f_c\frac{\mu_c}{\alpha} + (1 - f_c)\frac{\mu_f}{\alpha} = f_c\frac{\mu_s}{\alpha}$$

$$\frac{K' + \frac{4}{3}\mu'}{\alpha} = f_c\left(\frac{K_c + \frac{4}{3}\mu_c}{\alpha}\right) + (1 - f_c)\frac{K_f}{\alpha}. \tag{15}$$

Then porosity and density become

$$\phi = \frac{4\pi\alpha\varepsilon}{3}$$

$$\rho_b = (1 - \phi)\rho_m + (1 - f_c)\phi\rho_f + f_c\phi\rho_c. \tag{16}$$

Equation 15 is simply the Voigt average of the two fracture-filling materials. Accordingly, the original Hudson formulation would provide the same results if it were calculated simply by providing a Voigt average of the two fracture-filling materials.

Figure 2 shows distributions of P-wave velocities parallel (Vp_1) and perpendicular (Vp_2) to fractures and the fast (Vs_1) and slow (Vs_2) S-wave velocities. Distributions of fracture density and aspect ratio were used to provide the variations in velocity for a given cement percentage. The colors in each frame in Figure 2 correspond to distinct distributions, each to different fractions of cement.
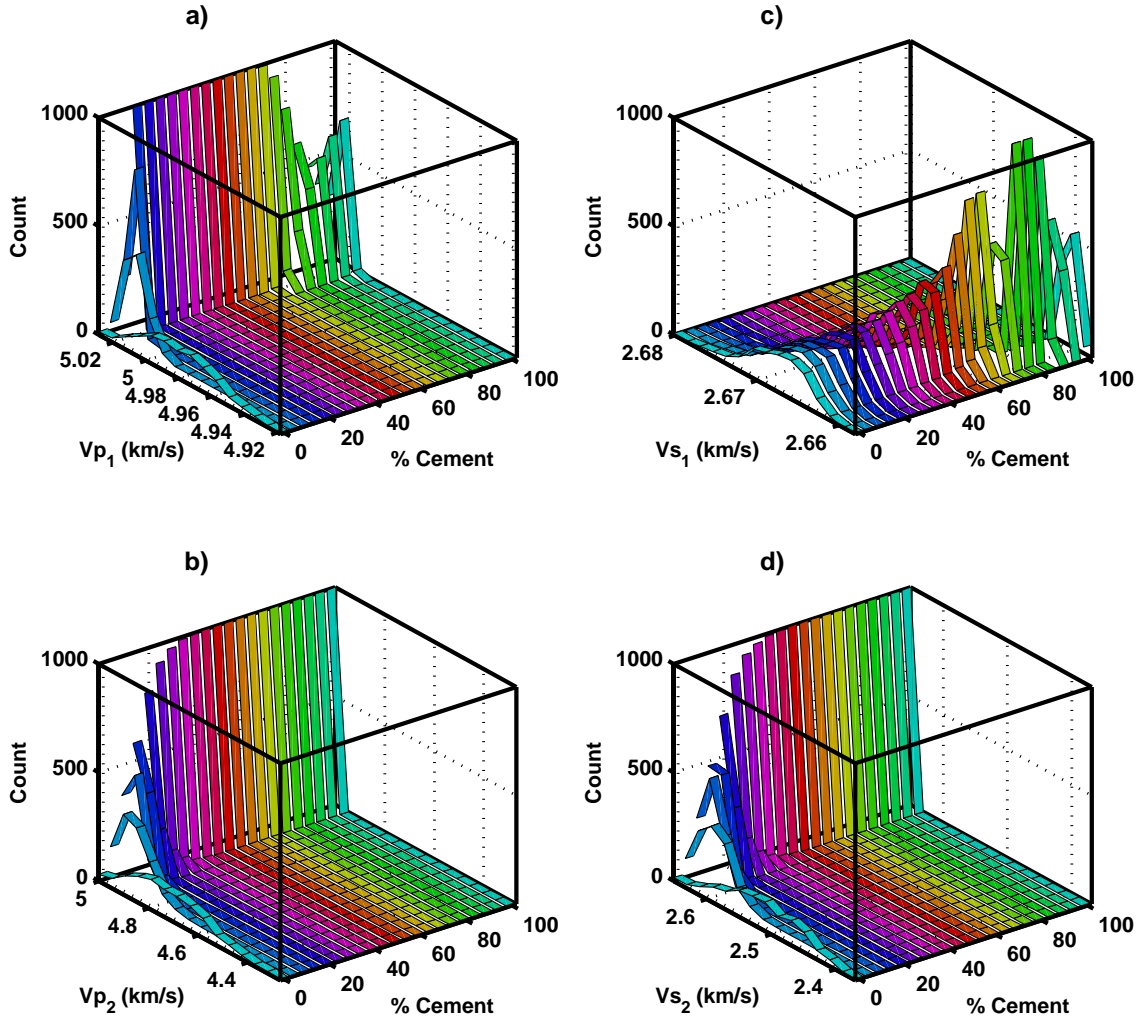
Figure 2. Fast and slow Vp (a and b) and fast and slow Vs (c and d) for different percentages of the fractures containing cement. The result is to treat the fracture-filling material as a Voigt average of the fluid and cement. For the slow Vp and Vs (b and d), just a few percent cement (less than 15%) makes the fast and slow Vp and Vs waves nearly identical.

The results in Figure 2 suggest that the first 10–15% of cement removes the apparent anisotropy in both P- and S-waves. For the Figure 2a, for P-waves parallel to fractures, little difference in velocity exists for any percentage of cement. In Figure 2b, velocities for cement less than about 10% show measurable differences to the corresponding values in Figure 2a. Similar results appear in the S-wave velocities (Figures 2c,d). Anisotropy constants (Thomsen, 1986) were also computed for the models generated from Equation 15 (Figure 3). For each different percentage of cement, the P-wave and S-wave anisotropic parameters ε_{ani} and γ_{ani}, respectively (Equations 17 and 18) are plotted as a function of aspect ratio, colored by fracture density. The maximum ε_{ani} (Figure 3, left) is approximately 0.35, which corresponds to 0% cement, with a moderate aspect ratio, but a relatively large fracture density (0.1). A maximum of 0.15 occurs for γ_{ani} (Figure 3, right) for 0% cement and high fracture density. Moving to percentages of cement greater than about 10% shows that the ε_{ani} and γ_{ani} drop to less than 0.05.

$$\varepsilon_{ani} = \frac{C_{11} - C_{33}}{C_{33}} \qquad (17)$$

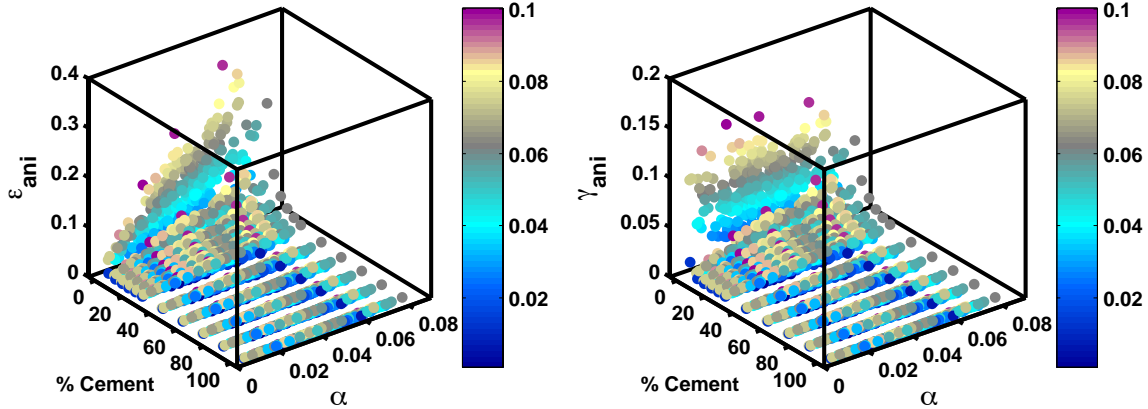$$\gamma_{ani} = \frac{C_{66} - C_{44}}{2C_{44}}. \qquad (18)$$

Figure 3. Thomsen anisotropic parameters epsilon (left) and gamma (right) showing the range of anisotropy as a function of cement fraction in the pore space, aspect ratio, and fracture density. For cement percentages greater than 10%, the directional dependence for the P- and S-waves is less than 0.05, which suggests that the background is nearly isotropic.

Figure 4 is a slightly different version of the anisotropy values. It provides a better way to visualize the diminishing amount of anisotropy as the cement percentage increases. P-wave anisotropy is plotted as a function of aspect ratio (left). Left is a plot of γ_{ani} versus aspect ratio. Color is the volume of cement (the same in both frames). Anisotropy increases as aspect ratio increases for all cement percentages less than 100%. Scatter is most prevalent in ε_{ani} and γ_{ani} for 0% cement, and that scatter consistently decreases as more cement is included. Although the results in Figures 2–4 indicate that small quantities of cement can minimize the observable HTI behavior, an effective fluid may not represent the true heterogeneous behavior a fracture system with some fractures fluid filled and others cement filled. The next approximation offers a slightly more robust argument to those presented in Equations 15.
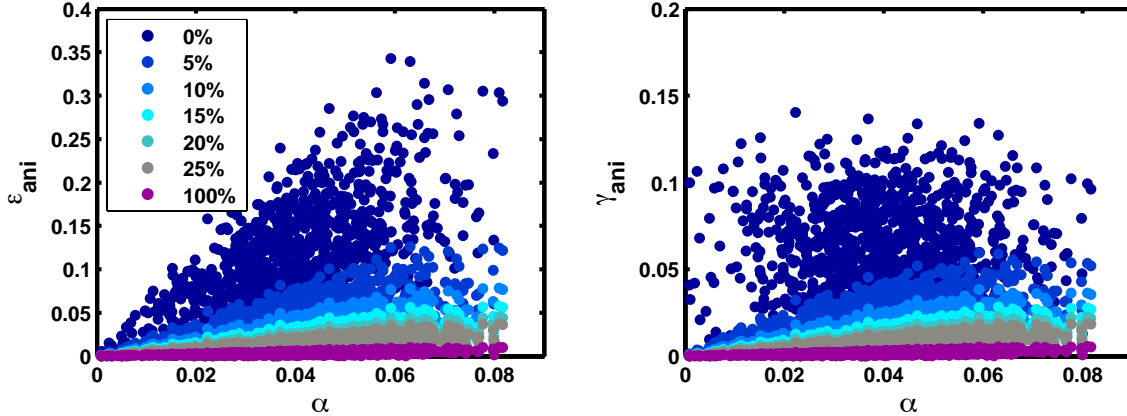
Figure 4. Thomsen anisotropic parameters epsilon (left) and gamma (right) showing the range of anisotropy as a function of aspect ratio for different cement volumes. Cement volumes range from 0–25% with a jump to 100%. As cement percentage increases, the amount of anisotropy in both epsilon and gamma parameters decreases.

Anisotropic superposition

This formulation uses the principle of superimposing a series of anisotropic corrections to an isotropic background, as does the Hudson model. However, two corrections are made, one for a set of cemented fractures and one for fluid-filled factures. These two sets of fractures do not have to have the same sets of fracture shapes and densities. More specifically, the collection of cement-filled fractures is allowed to have wider aperture (larger aspect ratios) and larger fracture densities than the fluid-bearing set. These wider and denser cement-filled fractures arguably are justified because the cement keeps the wider-aperture fractures open at depth. At the same time, the stiffer overall material could accommodate more fractures, allowing the fracture density to increase. The reformulation of Hudson's model in this manner is relatively straightforward. Separate definitions are provided for the effective stiffness for cement-filled (c_{ij}^c) and fluid-filled fractures (c_{ij}^f), where

$$
\begin{aligned}
c_{ij}^c &= c_{ij}^0 + c_{ij}^{1,c} \\
c_{ij}^f &= c_{ij}^0 + c_{ij}^{1,f}
\end{aligned}
. \tag{19}
$$

The effective stiffness ($c_{ij}^{eff,2}$) for these is a superposition of the background matrix, the effective stiffness with cement, and the effective stiffness with fluid:

$$
c_{ij}^{eff,2} = \left| c_{ij}^0 - c_{ij}^c \right| + c_{ij}^f . \tag{20}
$$

This formulation is an approximation. It is no longer exact because the first correction for cemented fractures makes the new background anisotropic. The advantage here, although the solution is not exact, is that the incorporation of variations in the quantity of cement does require

volumetric averaging of the fracture-filling material. Consequently, no mixing law (i.e., Voigt or Reuss) must be chosen. The c_{ij}^f term corresponds to 100% saturation in the fluid-filled fractures. To vary the quantity of cement, the aspect ratio and the fracture density are changed from the values used for the fluid-filled case (α_f and ε_f). The amount that the aspect ratio and fracture density are changed corresponds to the fraction of cement as

$$\begin{aligned} \alpha_c &= \alpha_f(\chi + f_c) \\ \varepsilon_c &= \varepsilon_f(\chi + f_c) \end{aligned} \quad , \tag{21}$$

where $\chi = 5$ is a scalar determined by numerical experimentation. Porosity is then computed by

$$\phi = f_c\phi + (1 - f_c)\phi = \phi_c + \phi_f, \tag{22}$$

where the volumes occupied by the cement and fluid are ϕ_c and ϕ_f, respectively. Using the relationship in the first formula in Equation 16, the total porosity is

$$\begin{aligned} \phi = \phi_c + \phi_f &= \frac{4\pi}{3}(\alpha_c\varepsilon_c + \alpha_f\varepsilon_f) \\ &= \frac{4\pi}{3}(\alpha_f\varepsilon_f(\chi + f_c)^2 + \alpha_f\varepsilon_f). \\ &= \frac{4\pi}{3}(\alpha_f\varepsilon_f[(\chi + f_c)^2 + 1]) \end{aligned} \tag{23}$$

Finally, the bulk density comes from the second formula in Equation 16.

When the superposition is calculated (Equation 18), the c_{ij}^c term is a function of α_c and ε_c. The argument for increasing these two parameters when cement is included is that cement-filled fractures with larger aspect ratios and fracture densities can exist where fluid-filled ones would be closed, and with lower fracture densities. Figure 5 illustrates the cases for fast and slow P-wave (a and b) and S-wave (c and d) velocities calculated from Equations 19–23. In Figure 5a, (Vp_1) very little change in velocity occurs as a result of either fractures or their fill, as expected. For Vp_2 (Figure 5b), the situation illustrates that including just 5% cement increases the apparent mean of the velocity by several hundred m/s. Continually increasing the cement percentage, however, does little to change this mean. The same behavior for P-waves is observed for S-waves. In Figure 5c, (Vs_1), little velocity change occurs with the addition of cement. In fact, the Vs1 velocity decreases, just slightly, when cement is included, as a function of density variations in the fracture-filling material. For Vs_2, a 5% increase in cement increases the mean velocity by about 100 m/s. Then Vs_2 changes little as the percentage of cement increases to 100%.
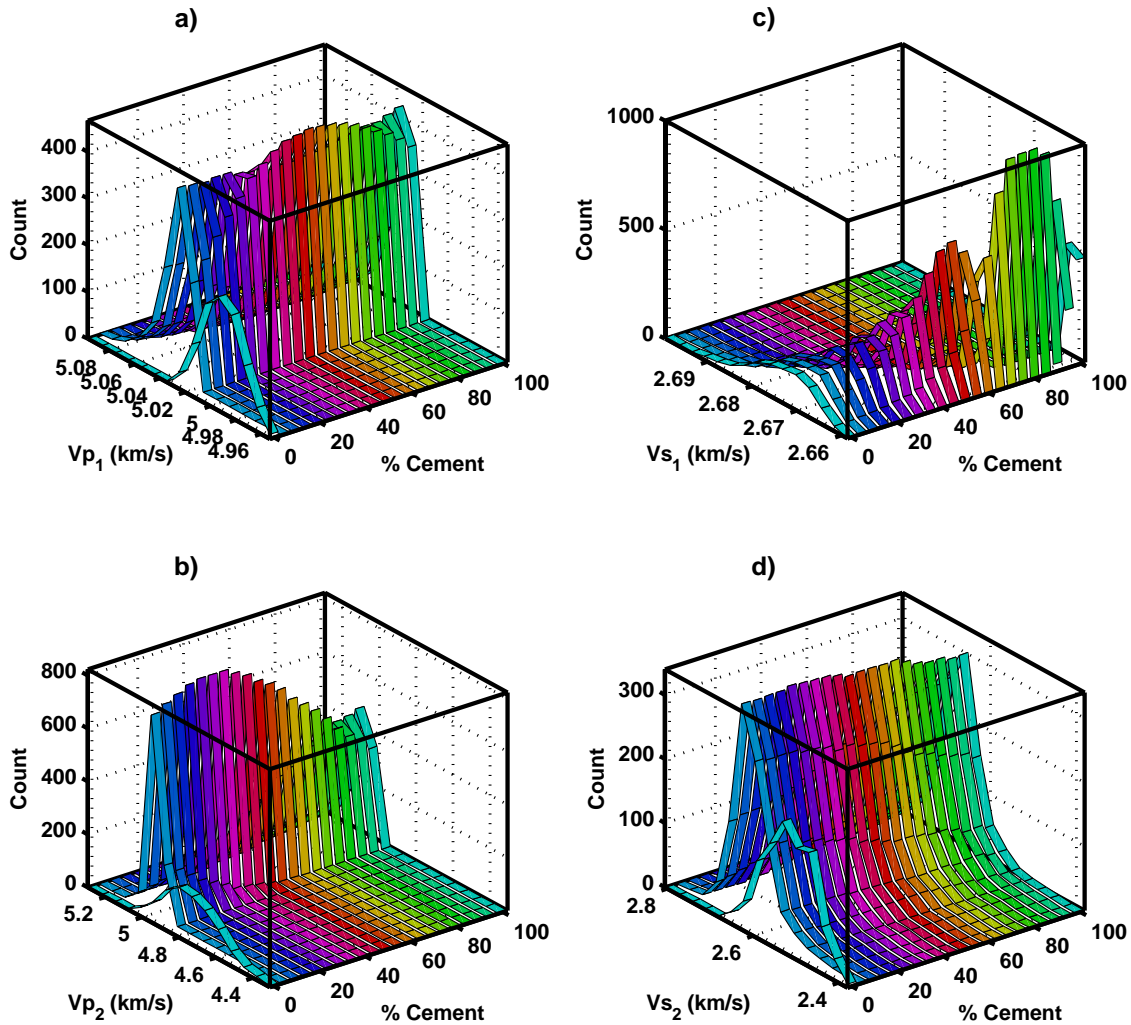
Figure 5. Fast and slow Vp and Vs for different percentages of cement, using Equations 19-23 to estimate an effective velocities by superimposing fluid- and cement-filled cases.

Considering the fluid-filled cases (0% cement) in Figures 5c and 5d, the difference in the mean is about 100 m/s. This difference easily could be observed in well-log data. The most interesting part of Figure 5c is not the quick increase of velocity with a small amount of cement. The interesting part is that even for a few percent cement, the slow and fast S-wave velocities are nearly the same. This is partly due to the increase in aspect ratio from the fluid case to the cemented cases. However, the change in aspect ratio and fracture density is not substantial from 0% cement to 5% cement (Figure 6). An increment of 1% cement showed similar results.
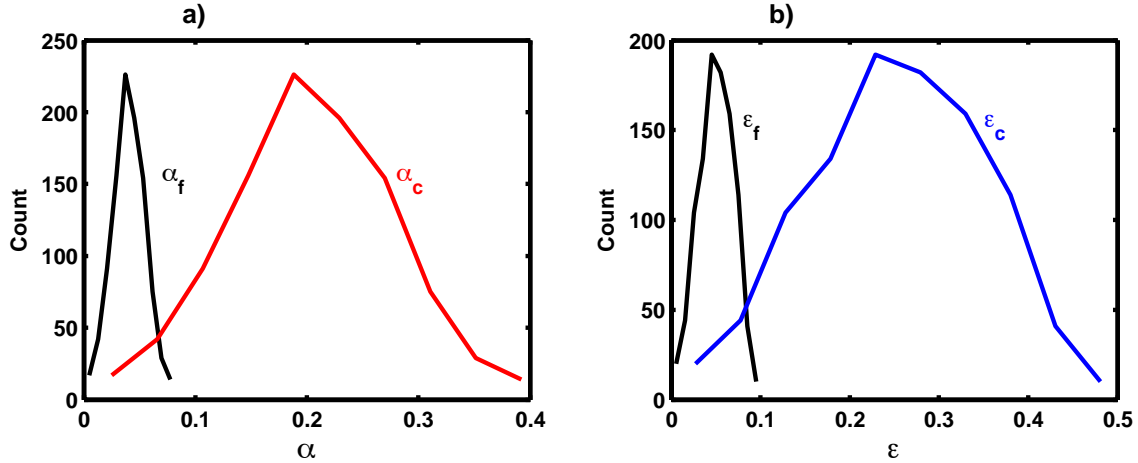
Figure 6. Aspect ratios (a) and fracture densities (b) for the fluid-filled, 0% cement case (black). Red in (a) and blue in (b) correspond to the 5% cement case. Abrupt changes in aspect ratio and fracture density from 0% to 5% cement partially explain the fast change in velocity in Figure 5.

Figures 7 and 8 demonstrate the abrupt changes in the P- and S-anisotropy terms. In both figures, ε_{ani} and γ_{ani} have relatively large values for 0% cement, over a range of aspect ratios. However, just 5% cement removes those noticeable trends, particularly for ε_{ani}. Figure 8 shows that minimal P-wave anisotropy is present for cement percent greater than zero, and ε_{ani} can become negative for certain values of aspect ratio. More scatter is present in γ_{ani} than in ε_{ani} for aspect ratios less than 0.1, but γ_{ani} also becomes negative for large aspect ratios. These negative values indicate that the aspect ratio controls the elastic response, with little contribution from the fracture-filling material.
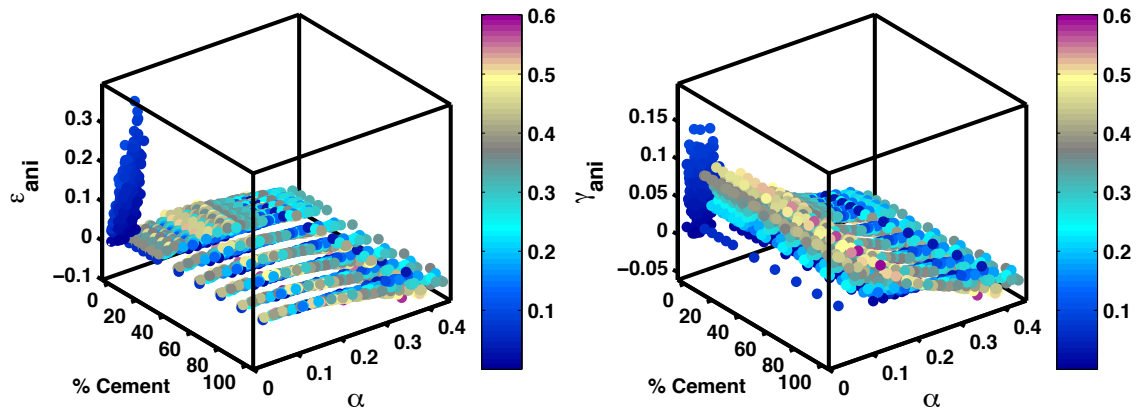

Figure 7. Anisotropic parameters computed from effective stiffnesses determined from superimposing a set of cemented fractures on a set of fluid-filled fractures. On the left is P-wave anisotropy as a function of cement percent and fracture shape, colored by fracture density. The right figure is the same except for S-wave anisotropy. Fracture density was allowed to exceed 0.1 where stiffer material with more cement is present.
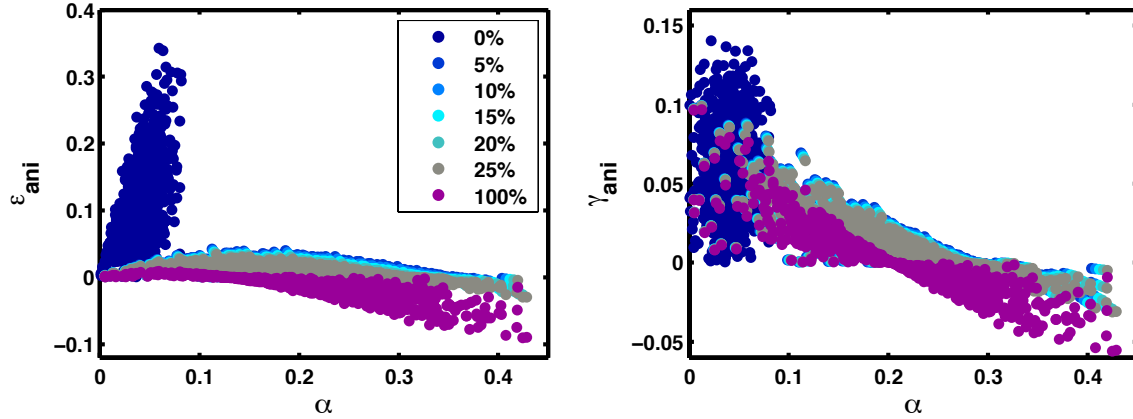
Figure 8. Thomsen anisotropic parameters epsilon (left) and gamma (right) showing the range of anisotropy as a function of aspect ratio for different cement volumes. These were calculated using stiffness elements in Equation 20. Cement volumes range from 0–25% with a jump to 100%. Both epsilon and gamma are noticeable for 0% cement, but they quickly fall off when including some cement. As cement percentage increases, the amount of anisotropy in both epsilon and gamma parameters decreases. Depending on the aspect ratio, both epsilon and gamma become negative for all cement percentages.

Cemented background material

Up to now, the consideration has been that an isotropic background is corrected with anisotropic corrections by placing different materials into the fractures or inclusions. Furthermore, the cement has been considered only part of the pore space. The next approach assesses the anisotropic stiffness when the cemented fractures are considered part of the matrix. This is the first step in recognizing that the background matrix may not always be isotropic. Although the modeling approach presented here ultimately relies on an isotropic background, I first discuss the issue of including an anisotropic background.

Anisotropic background

Nishizawa (1982), Mori and Tanaka (1973), Mura (1987), and Gavazzi and Lagoudas (1990) all extended Hudson's theory to include an anisotropic background. Importantly, Nishizawa (1982) required the anisotropic matrix to be aligned on the same symmetry axis as the set of fractures. In other words, if laminations resulted in VTI or HTI, then an associated set of fractures was aligned either horizontally (for VTI) or vertically (for HTI). Specifically, VTI media due to layering cannot be used as a background with vertical fractures. This assumption is key and most relevant to the work presented here. The case of an HTI background material that contains fracture oriented on the same symmetry axis matches the arguments for having two sets of fractures, one cemented and the other fluid filled. Although nine physical properties are needed (the same number as an orthorhombic system), those properties do not include anisotropic mineral moduli. The nine physical properties needed are the effective stiffnesses for the background HTI material (5 constants and density) plus the fracture-filling material (bulk and shear moduli and density). For fluid-filled fractures, this drops to eight.

14

Mura (1987), in a more general form than Nishizawa (1982) gave the analytic solution to the Eshelby tensor (strictly for a single inclusion) for a generic anisotropic background material in terms of a surface integral on a unit sphere (Equation 24).

$$S_{ijkl} = \frac{1}{8\pi} L_{0_{mnkl}} \int_{-1}^{1} d\psi_3 \int_{0}^{2\pi} [G_{imjn}(\bar{\vartheta}) + G_{jmin}(\bar{\vartheta})] d\omega \tag{24}$$

Equation 25 defines the individual terms in Equation 24.

$$G_{imjn}(\bar{\vartheta}) = \bar{\vartheta}_k \bar{\vartheta}_l N_{ij}(\bar{\vartheta}) / D(\bar{\vartheta})$$
$$\bar{\vartheta}_i = \psi_i / a_i; \quad \psi_1 = (1 - \psi_3^2)^{1/2} \cos\omega; \quad \psi_2 = (1 - \psi_3^2)^{1/2} \sin\omega; \quad \psi_3 = \psi_3; \tag{25}$$
$$D(\bar{\vartheta}) = \varepsilon_{mnl} K_{m1} K_{n2} K_{l3}; \quad N_{ij}(\bar{\vartheta}) \tfrac{1}{2} \varepsilon_{ikl} \varepsilon_{jmn} K_{km} K_{ln}; \quad K_{ik} = L_{0_{mnkl}} \bar{\vartheta}_j \bar{\vartheta}_l$$

Here, L_0 is the stiffness tensor, ε_{ijk} is the permutation tensor, and G_{ijkl} is Green's function. The a_i's are the axes of the ellipsoid aligned on a Cartesian grid. A numerical integration scheme (Gavazzi and Lagoudas, 1990) using a Gaussian quadrature formulation solves S_{ijkl} (Equation 26), which depends on the number of points to consider (M and N) over the two integration variables (ψ and ω, respectively). The Gaussian weights are W_{pq}.

$$S_{ijkl} = \frac{1}{8\pi} \sum_{p=1}^{M} \sum_{q=1}^{N} L_{0_{mnkl}} [G_{imjn}(\omega_q, \psi_{3p}) + G_{jmin}(\omega_q, \psi_{3p})] W_{pq} \tag{26}$$

Equation 24 can be solved analytically up to transverse isotropy conditions. For higher-order symmetry, Equation 26 is necessary. For numerical integration in Equation 26 to be useful, the nine properties aforementioned must be known as well as assigning values for W_{pq}. For transverse isotropy, and for a single inclusion, $M = 2$ and $N = 16$ (Gavazzi and Lagoudas, 1990). To extend this to multiple inclusions, these two numbers would have to be reevaluated, as would the Gaussian weights W_{pq}. Based on Eshelby's tensor and the numerical scheme in Gavazzi and Lagoudas (1990), the problem at hand is nearly solved. However, useful extensions of it have not been addressed. This is an area of future research.

Isotropic background

An approximation to the numerical scheme in Equation 26 is a statistical approach that treats the cement as part of the background or matrix material within the Hudson model. Thus, the assumption is that an isotropic background is sufficient. The statistical approach includes five correlations with associated uncertainty. They are between cement content and the 1) background stiffness, 2) background rigidity, 3) background density, 4) fracture density, and 5) the average fracture aspect ratio. These distributions represent the target distributions. Values were drawn from these to generate statistical distributions of stiffnesses from the Hudson model.

The relationships between cement fraction and background moduli were assigned to be logarithmic functions (Equations 35–36).

$$K_{\mathrm{M}} = \frac{\ln(f_c) + z_1}{z_2} + K_{\mathrm{cem}}^0$$

$$\mu_{\mathrm{M}} = \frac{\ln(f_c) + z_1}{z_3} + \mu_{\mathrm{cem}}^0 \tag{35}$$

where f_c is the fraction of cement. The variables z_i are coefficients defined as

$$z_1 = \left| \min(\ln(f_c)) \right|$$

$$z_2 = \frac{\max(\ln(f_c)) + z_1}{K_{\mathrm{cem}}^1 - K_{\mathrm{cem}}^0} \tag{36}$$

The terms K_{cem}^0 and K_{cem}^1 correspond to distributions of background moduli for cement fractions of 0 and 1, respectively. These distributions were normal, with means 38 and 71 GPa, respectively, and standard deviations 8 and 0.5 GPa, respectively. The same nomenclature is used for the shear moduli (μ). Mean values for rigidity were 38 and 17 GPa, with standard deviations 4 and 0.4 GPa, respectively. These statistical values allow for broad distributions when no cement is involved, with narrower and narrower distributions as cement increases. Figure 9a,b show a selection of realizations for K_M and μ_M. Two-dimensional histograms of the simulations are displayed in Figure 9c,d. The magenta and green lines are for the set of points that correspond to a set of matrix stiffness values where the mean values of z_1, K_{cem}^0, and K_{cem}^1 or z_1, μ_{cem}^0, and μ_{cem}^1 are used. This simply illustrates that simulations result in different expected values than those provided by using average values for variable in Equation 35. This mismatch between the magenta points and the high probability values (dark colors) increases as the standard deviations of the three distributions increases.
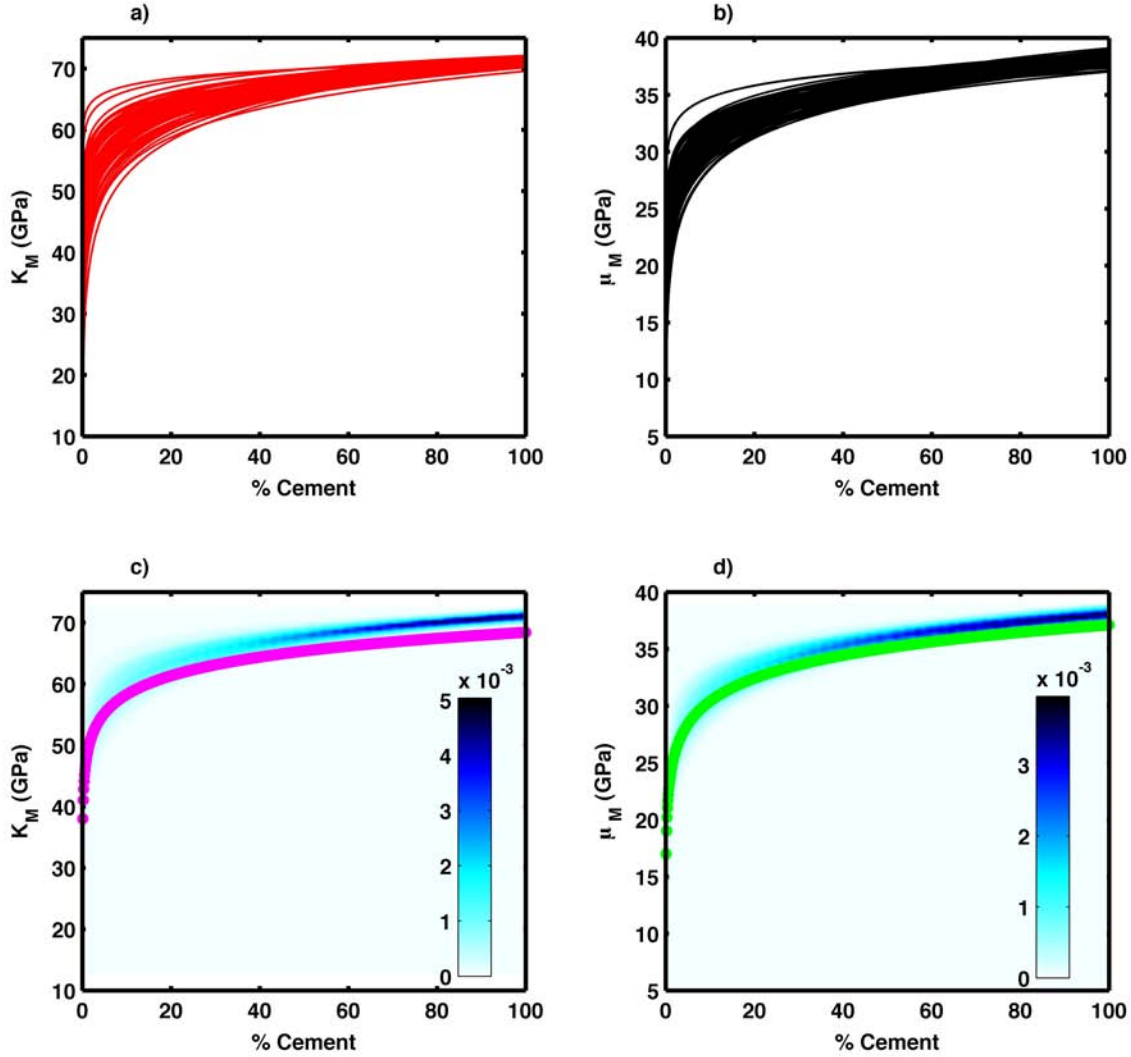
Figure 9. Correlated values of matrix bulk and shear moduli as a function of cement content. a) and b) are a selection of realizations. In c) and d), the corresponding bivariate PDFs in color. Magenta and green lines are the values obtained when using average properties as opposed to the simulation.

The last three sets of correlated variables are the matrix density, the fracture density, and aspect ratio. The latter two were defined as linear functions and set equal to each other. For no cement, the mean and standard deviations were 0.1 and 0.03, respectively; for 100% cement, they were 0.01 and 0.001, respectively (Figure 10). Density also was made a linear function of cement (Figure 11) with mean and standard deviation 2.48 and 0.03 g/cm^3, respectively for 0% cement. At 100% cement the mean was 2.71 g/cm^3 and the standard deviation 0.01 g/cm^3.
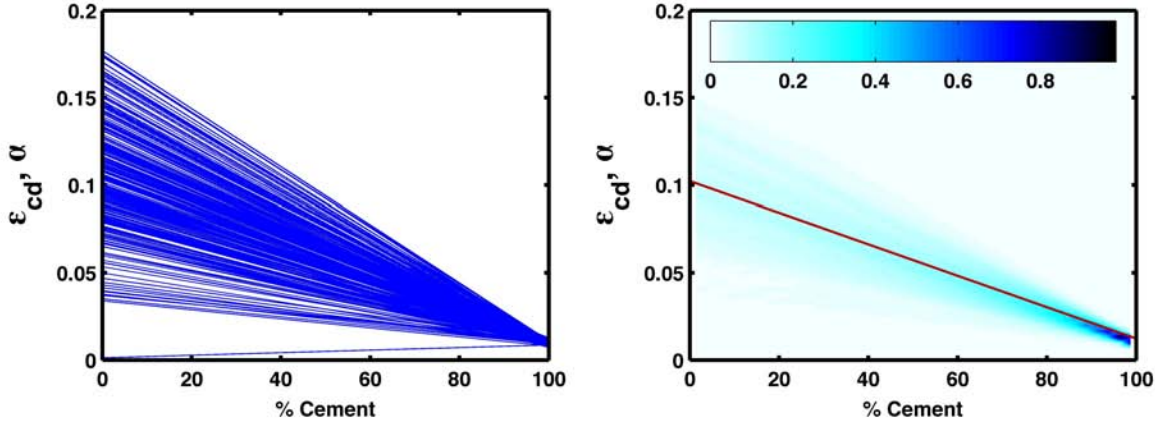
Figure 10. Correlated values of cement volume and fracture density and aspect ratio. The same distributions were used to define these two terms. However, during the drawing scheme, two independent drawings were performed.
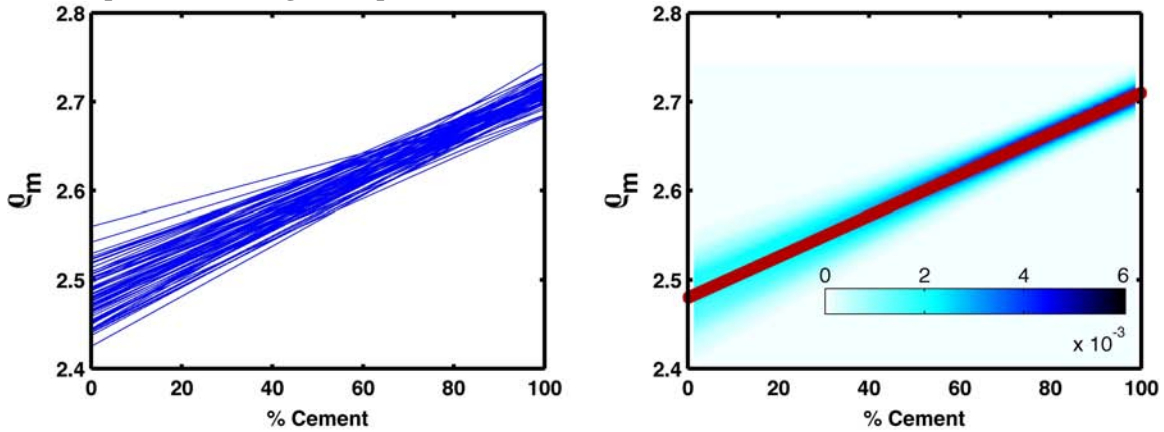

Figure 11. Density was linearly correlated with cement volume. The 100% cement point corresponds to pure calcite. The 0% cement point was set at an arbitrary but realistic value.

Implementation of these distributions means that for a given value of f_c, at least one value of each property is drawn from its respective distribution. Accordingly, a uniform distribution of f_c was defined between 0% and 100%. Three hundred values were assigned within this uniform distribution. For each value of f_c, 20 values of each of the five correlated properties were drawn. These values were then used to compute a realization within the Hudson model. The number of realizations totaled 6000. Figure 12 displays the fast and slow P-wave velocities (left) and S-wave speeds (right). Similar to the results shown in Figure 2–8, all velocities increase, as expected, as the amount of cement increases. The fast P-wave velocities (red) show a relatively narrow distribution for all f_c. However, the slow P-waves (black) exhibit substantial scatter. For the S-waves, both show approximately the same scatter but with slightly different mean values.
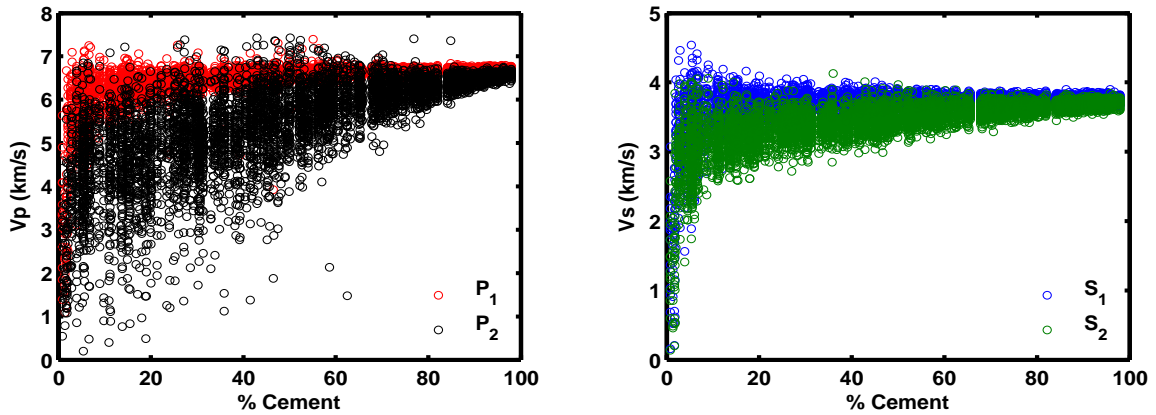
Figure 12. Anisotropic velocities as a function of cement content. On the left are fast (red, P_1) and slow (black P_2) P-wave speeds. The slow P-wave data shows considerable scatter relative the fast P-wave. Blue on the right is fast S-wave velocity, and green is for the slow S-wave. Overlap is present in both plots. However, this overlap is more significant for the S-wave data.

The overlap in Figure 12 is the focus here because it explains the minimal difference between the fast and slow waves. A different plot style (Figure 13) shows the velocity distributions for the P-waves. On the left, the bivariate PDF is colored by the joint probability (same as the vertical axis). The right picture in Figure 13 contains the same PDFs (one for the fast and one for the slow P-wave), colored with a single shade. These distributions show the overlap more clearly than does Figure 12 (left). Figure 14 contains plots of S-wave velocity, cement percent, and their joint probability. Of particular interest in this figure is the overlap, which is more significant in the P-wave velocities. At 0% cement, the mean velocities differ by ~100 m/s. This difference is observable in real well log data. To discern this in seismic data may be more difficult. However, these modeling results arguably are useful for explaining the lack of shear-wave splitting in well log data from shale reservoirs.
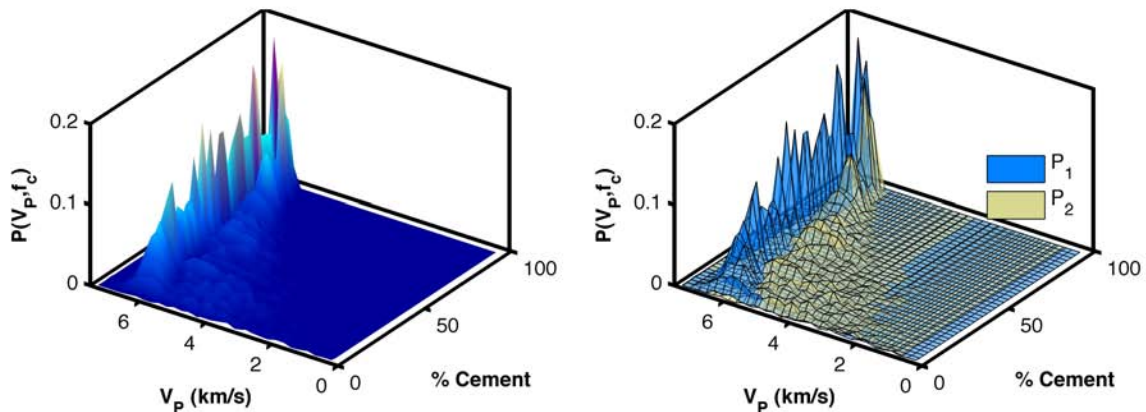

Figure 13. P-wave velocity distributions on the left and right for both fast (P1) and slow (P2) modes. The distributions are colored by joint probability on the right, where color is the same as the z-axis. On the left, the two distributions are colored individually to demonstrate the overlap between them. The overlap is the least for no cement but significant for cement >40%.
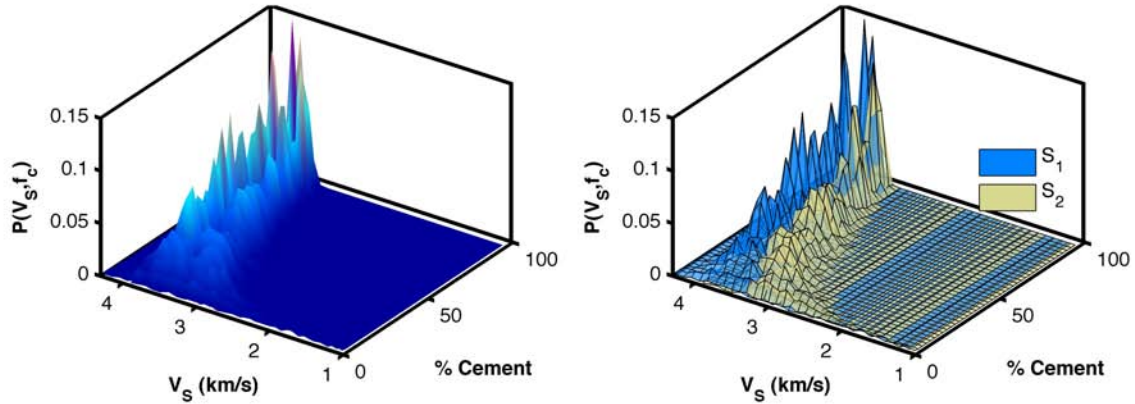
Figure 14. S-wave velocity distributions. On the left, the fast and slow S-wave velocity distributions are colored by their joint probabilities as a function of cement and velocity. On the right, the same distributions are plotted, but the colors correspond to S1 (blue) and S2 (yellow).

CONCLUSIONS

This work presented three approaches to modeling cement content in a fractured medium. Each demonstrates the ability to explain the minimal or the absence of azimuthal variation in log-based S-wave velocities within shale gas units that are known to show horizontal transverse isotropy. The first and second approaches place the cement along with the fluid in the fracture porosity. The third treats the background material as having variable cement content, along with fluid-filled fractures. All three approaches are extensions of the Hudson fracture model, but the complexity increases from the first to third approaches. In addition, the number of inputs to include grows with each particular technique. All three are straightforward to implement. However, experimental validation of any of the models requires comparing their calibrated predictions to real velocity measurements. This would include knowing the cement content for the real rock for a proper calibration, which is one are of active research.

These modeling approaches allow for reconciling the observed HTI behavior in surface seismic data that does not always appear in well log velocity data. This is important to recognize because any quantitative interpretation or joint inversion of seismic and well data requires inputs from both measurement types. Considering both data types may also include addressing the issue of fracture scale (spacing and size), or even more complicated, accounting for true orthorhombic symmetry. Accounting for orthorhombic symmetry at either the seismic or log scale may prove quite challenging. The third modeling approach presented in this paper may prove useful for an HTI scenario where cement content and fracture spacing are both included to explain seismic-scale HTI but a no azimuthal dependence at the well-log scale. Finally, this work illustrates the application of effective medium models to explain increasingly complex rocks in terms of elasticity. These effective medium predictions currently are being compared to velocities and moduli obtained from numerical propagation simulations in complex media. These types of comparison are a new research venture that will help validate the application of effective medium models to complex systems such as fractured gas shales.

ACKNOWLEDGMENTS

REFERENCES

Andrews, R.D, 2009, Production decline curves and payout threshold of horizontal Woodford wells in the Arkoma Basin, Oklahoma: the journal of the Oklahoma City geological society, 103-111.

Avseth, P., T. Mukerji, and G. Mavko, 2005, Quantitative seismic interpretation: Applying rock physics tools to reduce interpretation risk: Cambridge University Press.

Budiansky, B. and R. J. O'Connell, 1976, Elastic moduli of a cracked solid: International Journal of Solids and Structures, **12**, 81–97.

Cheng, C. H., 1993, Crack models for a transversely anisotropic medium: Journal of Geophysical Research, **98**, 675–684.

Doyen, P., 2007, Seismic reservoir characterization: EAGE.

Engelder, T., Lash, G.G. and Uzcátegui, R.S., 2009, Joint sets that enhance production from middle and upper Devonian gas shales of the Appalachian basin: AAPG Bulletin, **93**, 7, 857-889.

Eshelby, J. D., 1957, The determination of the elastic field of an ellipsoidal incisions, and related problems: Proceedings of the Royal Society of London, **241**, 379–396.

Gavazzi, A. C. and D. C. Lagoudas, 1990, On the numerical evaluation of Eshelby's tensor and its application to elasoplastic fibrous composites: Computational Mechanics, **7**, 13–19.

Hudson, J. A., 1980, Overall properties of a cracked solid: Mathematical proceedings of the Cambridge Philosophical Society, **88**, 371–384.

Hudson, J. A., 1981, Wave speeds and attenuation of elastic waves in material containing cracks: Geophysical Journal of the Royal Astronomical Society, **64**, 133–150.

Hudson, J. A., 1994, Overall properties of anisotropic materials containing cracks: Geophysical Journal International, **116**, 279–282.

Jakobsen, M., J. A. Hudson, and T. A. Johansen, 2003, T-matrix approach to shale acoustics: Geophysical Journal International, **154**, 533–558.

Kahraman, S., 2002, Correlation of TBM and drilling machine performances with rock brittleness: Engineering Geology, **65**, 269–283

Kuster, G. T. and M. N. Toksöz, 1974, Velocity and attenuation of seismic waves in two-phase media: Geophysics **39**, 587–618.

Mori, T. and K. Tanaka, 1973, Average stress in matrix and average energy of materials with misfitting inclusions: Acta Metallurgica, **21**, 571–574.

Mura, T, 1987, Micromechanics of defects in solids 2nd edition: Dordrecht: Martinus Nijhoff.

Nishizawa, O, 1982, Seismic velocity anisotropy in a medium containing oriented cracks – transversely isotropic case: Journal of the Physics of he Earth, 30, 331–347.

Norris, A. N., 1985, A differential scheme for the effective moduli of composites: Mechanical Materials, **4**, 1–16.

Portas, R. M., and Slatt, R., 2010, Characterization and origin of fracture patterns in a Woodford shale quarry in Southeastern Oklahoma for application to exploration and development: AAPG search and discover article #90104, AAPG annual convention and exhibition.

Sayers, C. M., A. D. Taleghani, and J. Adachi, The effect of mineralization on the ratio of normal to tangential compliance of fractures: Geophysical Prospecting, **57**, 439–446.

Thomsen, L., 1986, Weak elastic anisotropy: Geophysics, **51**, 1954–1966.